

Journal of Biomedical Optics

BiomedicalOptics.SPIEDigitalLibrary.org

Nanoscale photoacoustic tomography for label-free super-resolution imaging: simulation study

Pratik Samant
Timothy A. Burt
Zhizhuang Joe Zhao
Liangzhong Xiang

SPIE.

Pratik Samant, Timothy A. Burt, Zhizhuang Joe Zhao, Liangzhong Xiang, "Nanoscale photoacoustic tomography for label-free super-resolution imaging: simulation study," *J. Biomed. Opt.* **23**(11), 116501 (2018), doi: 10.1117/1.JBO.23.11.116501.

Nanoscale photoacoustic tomography for label-free super-resolution imaging: simulation study

Pratik Samant,^a Timothy A. Burt,^b Zhizhuang Joe Zhao,^c and Liangzhong Xiang^{d,*}

^aUniversity of Oklahoma, Stephenson School of Biomedical Engineering, Norman, Oklahoma, United States

^bUniversity of Oklahoma, Homer L. Dodge Department of Physics and Astronomy, Norman, Oklahoma, United States

^cUniversity of Oklahoma Health Sciences Center, Department of Pathology, Oklahoma City, Oklahoma, United States

^dUniversity of Oklahoma, School of Electric and Computer Engineering, Norman, Oklahoma, United States

Abstract. Resolutions higher than the optical diffraction limit are often desired in the context of cellular imaging and the study of disease progression at the cellular level. However, three-dimensional super-resolution imaging without reliance on exogenous contrast agents has so far not been achieved. We present nanoscale photoacoustic tomography (nPAT), an imaging modality based on the photoacoustic effect. nPAT can achieve a dramatic improvement in the axial resolution of the photoacoustic imaging. We derive the theoretical resolution and sensitivity of nPAT and demonstrate that nPAT can achieve a maximum axial resolution of 9.2 nm. We also demonstrate that nPAT can theoretically detect smaller numbers of molecules (~273) than conventional photoacoustic microscopy due to its ability to detect acoustic signals very close to the photoacoustic source. We simulate nPAT imaging of malaria-infected red blood cells (RBCs) using digital phantoms generated from real biological samples, showing nPAT imaging of the RBC at different stages of infection. These simulations show the potential of nPAT to nondestructively image RBCs at the nanometer resolutions for *in vivo* samples without the use of exogenous contrast agents. Simulations of nPAT-enabled functional imaging show that nPAT can yield insight into malarial metabolism and biocrystallization processes. We believe that the experimental realization of nPAT has important applications in biomedicine. © 2018 Society of Photo-Optical Instrumentation Engineers (SPIE) [DOI: 10.1117/1.JBO.23.11.116501]

Keywords: photoacoustic imaging; super-resolution imaging; functional imaging; label-free imaging; red blood cells; malaria.

Paper 180384R received Jun. 27, 2018; accepted for publication Oct. 12, 2018; published online Nov. 8, 2018; corrected Sep. 17, 2019.

1 Introduction

Super-resolution imaging has pushed past the optical diffraction limit and revolutionized optical imaging at the cellular and molecular levels.¹ Many imaging modalities have been successful in achieving high-resolution imaging of biological samples, meeting or exceeding resolutions required for single-cell imaging.²⁻⁴ Conventional super-resolution imaging techniques work by first labeling the region of interest with fluorophores, and then precisely determining the distribution of these fluorophores to form an image.⁵⁻⁷ The high resolution provided by fluorescence imaging techniques has been a crucial feature leading to multiple biomedical discoveries⁸⁻¹¹ by probing at length scales previously inaccessible to optical imaging. However, fluorescence-based super-resolution techniques rely on exogenous fluorophores to image at high resolutions. Therefore, these techniques often suffer from limited imaging times due to photobleaching and can result in sample damage through phototoxicity effects. Lastly, optical scattering in tissue remains a large problem, which limits imaging depth.¹²

One important context in which high-resolution imaging can yield important biomedical insight is that of malarial development in red blood cells (RBCs). Malaria remains a worldwide problem causing >400,000 deaths each year. Therefore, the understanding of malarial metabolism and development has global impetus.¹³ Entering the blood stream from the bite of an infected *Anopheles* mosquito, the malaria parasite (*Plasmodium falciparum*) infects human RBCs, where it metabolizes

hemoglobin (Hb) and grows, before eventually causing cell membrane rupture and enters the blood stream. Invasion by *P. falciparum* can be characterized in infected RBCs via the presence of hemozoin (Hz). The malaria parasite, while inside the RBC, consumes up to 80% of the host cell's Hb.¹⁴ This Hb is digested by the parasite, releasing toxic heme byproducts. To prevent cell lysis, the parasite processes these toxic heme groups via biocrystallization into Hz crystals, which are inert.¹⁵⁻¹⁷ It is well known that the mechanism of the action of frontline anti-malarial drug Chloroquinone is the inhibition of the Hz formation in the digestive vacuole of malaria.¹⁸ Important information regarding malarial metabolic activity and drug efficacy can be gained by quantifying Hz and Hb concentrations throughout the cell. However, the erythrocytic development of malaria happens on length scales much smaller than the 8- μ m diameter of erythrocytes. *P. falciparum* merozoites are typically 1.5 microns in diameter,¹⁹ and metabolized molecules such as Hb have an average diameter of 5.5 nm.²⁰ Therefore, to image malarial metabolism and Hb digestion progress, resolutions well below 1.5 μ m are desired, as resolutions approaching the size of single Hb molecules can provide important insight into macromolecular processes such as Hz biocrystallization and effectiveness of antimalarial agents. The most common form of malarial microscopy remains blood films, as major parasite species are distinguishable in these tests. However, blood films require the removal of blood from the host, and additional staining followed by imaging via conventional light microscopy. Blood film microscopy cannot perform dynamic imaging and has only

*Address all correspondence to: Liangzhong Xiang, E-mail: xianglzh@ou.edu

diffraction limited resolutions. Therefore, it is not sufficient for the visualization of molecular processes. Super-resolution, label-free imaging as required for research purposes is not achievable with blood film microscopy.

Photoacoustic microscopy (PAM) is a promising biomedical imaging modality, which can overcome the traditional limits of optical diffusion by taking advantage of the photoacoustic effect and, instead, by detecting an optically induced acoustic signal.¹² However, PAM's axial resolution is limited because conventional piezoelectric transducers have difficulty in detecting GHz frequency acoustic signals, which encode higher resolution information. Whereas progress has been made in the development of high-frequency transducers,^{21,22} transducers that can sensitively detect signals in the range of several GHzs are not commonly available commercially. Among high bandwidth transducers that are available, high acoustic frequency attenuation due to the large distance between the source and the detector remains a problem.²³

Consequently, there does not yet exist an imaging modality that can achieve super-resolution imaging without reliance on fluorescent labeling and also overcome high optical scattering effects in tissue. Label-free super-resolution imaging remains a technological challenge. Here, we present the capabilities of nanoscale photoacoustic tomography (nPAT), a biomedical imaging modality that can achieve nanometer-level resolutions and optical contrast without reliance on fluorescent labeling. nPAT takes advantage of the photoacoustic effect to generate ultrasound signals generated via optical absorption. In this way, nPAT encodes optical contrast information in an ultrasonic signal. This high-frequency ultrasound can yield super-resolution (better than 200 nm) imaging in the axial direction of laser excitation. This is accomplished by detecting acoustic signals in the GHz range by taking advantage of pump-probe techniques commonly used in picosecond ultrasonics.

According to theoretical models, nPAT is capable of high-resolution *in vivo* imaging of malarial development at different stages. nPAT can yield anatomical and functional information as the distribution of Hb throughout the cell can reveal both the outline of malarial parasites as well as their metabolic activity. In this paper, we calculate the theoretical resolution and sensitivity of an nPAT imaging technique. We then simulate nPAT imaging of malaria-infected RBCs in both early and late stages of the blood-stage life cycle. We compare the imaging features of nPAT with those of x-ray microscopy and demonstrate the simultaneous anatomic and functional imaging capabilities of nPAT.

2 Theory of Nanoscale Photoacoustic Tomography

2.1 Principle of Nanoscale Photoacoustic Tomography

nPAT uses two laser beams for signal generation and detection. The excitation beam is tuned to an absorbance peak of the primary molecule being used as a contrast agent (532 suffices in the case of Hb). The excitation and detection wavelengths are kept below the ANSI safety limit if dynamic imaging of biological samples is desired. The detection beam is ideally tuned to a wavelength of maximum reflectance but can also be of the same wavelength as the excitation wavelength. Pump-probe detection of the excitation beam-induced acoustic signal is then performed in the axial direction.^{24,25} Optical detection as

opposed to detection by an ultrasound transducer enables nPAT to detect extremely high-frequency signals.²⁵⁻²⁹ This allows for nPAT's axial resolution to surpass that of conventional PAM as the axial resolution is dependent on the bandwidth of ultrasound detection.³⁰ This extends the theoretical resolution of nPAT into the nanometer range. The high resolution achieved by nPAT is not a result of optical focusing, but instead the extremely high bandwidths that are achievable in laser-based pump-probe systems. As a result, the resolution of nPAT should ultimately only depend on the excitation pulse duration and sound velocity.

The experimental setup of nPAT requires the use of a pulsed laser, several beam splitters, two focusing lenses of sufficiently high numerical aperture, an optical delay line, mirrors, and detection electronics (e.g., photodiodes). The laser beams are close to confocal on the sample, with the pump being less finely focussed than the probe so as to enable a large axial field of view. A schematic of an nPAT setup is available in our previous studies.²⁴

The primary axial resolution limitations in current photoacoustic imaging techniques such as PAM are the bandwidth of the detecting ultrasound transducer and the laser pulse duration.³⁰⁻³³ Typical transducers are capable of detecting photoacoustic signals on the order of tens of MHz. However, the physical photoacoustic signal is theoretically broadband, with relevant contributions in the GHz range for excitation pulses on the order of picoseconds.³⁴ These GHz signals contain information about higher resolution imaging, and the ability to detect them is directly tied to the resolution of the final image. Therefore, to detect such high-frequency pulses and obtain nanometer resolution in the axial direction, a piezoelectric transducer is insufficient. For this reason, nPAT uses a pump-probe signal detection method, allowing for the detection of high bandwidths.

2.2 Resolution of Nanoscale Photoacoustic Tomography

To calculate the maximum achievable resolution of nPAT, we begin by considering the excitation pulse laser. For a Gaussian laser pulse, the intensity as a function of time can be written as

$$I(t') = \frac{E_0}{\theta} \exp\left[k \frac{-t'^2}{\theta^2}\right], \quad (1)$$

where $t' = 0$ at the instant of maximum intensity, θ is the laser pulse duration, $k = 4 \ln 2$, and E_0 is the fluence of the laser pulse. We assume that this laser pulse is incident on a point absorber. At some distance r from the point absorber, the center of the resultant acoustic pulse will arrive at a time $t = t' + r/v$, where v is the speed of sound in the medium.

Let $\tau = \frac{(t-r)}{\theta}$. Then, substituting this into Eq. (1):

$$I(\tau) = \frac{E_0}{\theta} \exp\left[k \frac{-(t-\frac{r}{v})^2}{\theta^2}\right] = \frac{E_0}{\theta} \exp[-k\tau^2]. \quad (2)$$

The photoacoustic pressure produced by a point source as a function of r and τ has been derived by Calasso et al.³⁵ In the case of delta function heating and linear thermal expansion, it is given as

$$P(\tau, r) = \frac{\sigma\beta}{4\pi\theta c_p r} \left[\frac{d}{d\tau} I(\tau) \right]. \quad (3)$$

Substituting in Eq. (2) into Eq. (3) yields

$$P(\tau, r) = \frac{E_0\sigma\beta}{4\pi\theta^2 c_p r} \left[\frac{d}{d\tau} \exp(-k\tau^2) \right] = \frac{-E_0\sigma\beta k\tau}{2\pi\theta^2 c_p r} \exp[-k\tau^2], \quad (4)$$

where σ is the optical cross section of the particle, c_p is the specific heat capacity of the medium, and β is the coefficient of thermal expansion.

This function has maxima/minima at $\tau = \pm \frac{1}{\sqrt{2k}}$, which corresponds to $t = \pm \frac{\theta}{\sqrt{2k}} + \frac{r}{c}$. Applying the Rayleigh criterion, the temporal diffraction limit of two such point sources will occur when the minimum pressure of one point signal coincides with the maximum pressure of another. This is equivalent to the distance between the maximum and minimum of the photoacoustic point source. Time between the maxima and minima is then $\frac{2\theta}{\sqrt{2k}}$. The Rayleigh spatial resolution is given by converting this time into a distance by multiplying by the sound speed. Then, the maximum theoretical resolution achievable by a point source is given as

$$R = \frac{2\theta v}{\sqrt{2k}}. \quad (5)$$

For a pulse duration of 7 ps and $v = 1549.3$ m/s, this corresponds to a maximum achievable axial resolution of 9.2 nm.

2.3 Sensitivity of Nanoscale Photoacoustic Tomography

The sensitivity of nPAT is an important parameter in the assessment of its potential. Whereas an ultrasonic transducer benefits from higher sensitivities at the cost of lower bandwidth, acoustic detection via a laser pulse is the opposite scenario. The sensitivity of probe laser detection will be less than that of an ultrasound transducer at comparable distances from the source. The probe beam acts similar to a high-bandwidth transducer, and detects acoustic waves at the point at which it is focused. In this way, the focused probe beam can detect acoustic waves traveling through the focal point, and the pump beam can generate these acoustic waves. The two beams, pump and probe, can be focused very close to each other, making it easier to detect an nPAT signal very close to the source as compared with PAM. The sensitivity of nPAT can be estimated based on the theoretical change in refractive index caused by the acoustic pressure.

We assume that the sound wave (for simplicity's sake) is a box function in one-dimension and propagates outward in three-dimensions. Then, the resultant change in refractive index induced related to the wave intensity is given as³⁶

$$\Delta n_0 = \frac{1}{2} \hat{p} n^3 \sqrt{\frac{2I_a}{\rho v^3}}, \quad (6)$$

where \hat{p} is the photoelastic tensor, n is the refractive index, ρ is the density of the material, and I_a is the acoustic intensity. The acoustic intensity is equal to the acoustic power divided by the distributed area. For a spherical wave, this corresponds to

$$I_a = \frac{\text{Power}}{\text{Area}} = \frac{AP^2}{\rho c A} = \frac{P^2}{\rho v},$$

where A is the surface area of the sphere, and P is the pressure. Then

$$\Delta n_0 = \frac{1}{2} \hat{p} n^3 \sqrt{\frac{2P^2}{\rho^2 v^4}} = \frac{\sqrt{2}}{2} \hat{p} n^3 \frac{P}{\rho v^2}, \quad (7)$$

where \hat{p} is related to the material parameter, M , as follows:³⁶

$$M = \frac{\hat{p}^2 n^6}{\rho v^3}. \quad (8)$$

It is assumed that M for water and blood plasma remains the same. We also know that, for blood plasma, $\rho = 1025$ kg/m³, $v = 1549.3$ ms⁻¹, $n = 1.333$ using 532-nm light. This corresponds to $\hat{p} = 10.5$.

Simulations have suggested that acoustic waves produced by RBCs can reach amplitudes as high as 2500 pa.³⁴ For such a pressure, the resulting change in the refractive index is $\Delta n_0 = 1.775 \times 10^{-5}$. In pump-probe imaging, the corresponding reflectance change, δR , induced by Δn_0 is the probed quantity and can be given by evaluating the usual Fresnel equation

$$\delta R = R_2 - R_1 = \left| \frac{n_a - (n_b - \Delta n_0)}{n_a + n_b} \right|^2 - \left| \frac{n_a - n_b}{n_a + n_b} \right|^2, \quad (9)$$

where n_a is the refractive index in the air (~ 1) and n_b is the refractive index in the medium.

Substituting Eqs. (7) and (8) into Eq. (9) yields $\delta R \approx -2.17 \times 10^{-6}$. If instead we wish to go in the opposite direction and calculate the minimum detectable pressure (i.e., the sensitivity of nPAT), then we must isolate for pressure. Rearranging Eq. (9), we have

$$\sqrt{\delta R + \left| \frac{n_a - n_b}{n_a + n_b} \right|^2} = \left| \frac{n_a - (n_b - \Delta n_0)}{n_a + n_b} \right|. \quad (10)$$

As $n_a - n_b = 0.333$, and the magnitude of Δn_0 will not exceed 0.333 (this would correspond to a pressure of 46 MPa, which is unreasonably high), the right side will be negative prior to taking the absolute value. Then, substituting in Eqs. (7) and (8) into Eq. (9) provides an equation for the pressure, as follows:

$$\begin{aligned} -\sqrt{\delta R + \left| \frac{n_a - n_b}{n_a + n_b} \right|^2} &= \frac{n_a - (n_b - \Delta n_0)}{n_a + n_b} \\ -(n_a + n_b) \sqrt{\delta R + \left| \frac{n_a - n_b}{n_a + n_b} \right|^2} - n_a + n_b &= \Delta n_0 \\ &= \frac{\sqrt{2}}{2} \hat{p} n_b^3 \frac{P}{\rho v^2} \\ P &= \frac{\sqrt{2} (-(n_a + n_b) \sqrt{\delta R + \left| \frac{n_a - n_b}{n_a + n_b} \right|^2} - n_a + n_b) \rho v^2}{P n_b^3}. \end{aligned} \quad (11)$$

The pump–probe method’s sensitivity to reflectivity is theoretically limited to a reflectivity ratio change on the order of -10^{-6} , which corresponds to a reflectance change of $\delta R = 2.04 \times 10^{-8}$.³⁷ Substituting this into Eq. (11) yields a noise equivalent pressure (NEP) of 21 pa, whereas ultrasound transducers can detect pressures as small as <1 Pa.³⁸

The number of molecules (NEN) required to generate this pressure, known as the noise equivalent NEN, is given by dividing this pressure by the pressure generated by a single molecule, p_s .³² For Hb, this pressure is given by the equation

$$p(r) = \frac{E_0 \sigma_{Hb} \beta}{4\pi \theta^2 c_p r}. \quad (12)$$

However, Eq. (12) does not hold for indefinitely small pulse widths, and at pulse widths extending to shorter than stress confinement, the dependence on pulse-width vanishes, with shorter pulse widths no longer increasing signal amplitude.³² As compared with PAM, which uses an ultrasonic transducer, nPAT will benefit from typically higher NEN due to the fact that nPAT’s pump–probe detection method allows for r to be very close to the source itself. However, laser-based detection is less sensitive than an ultrasound transducer at comparable distances from the source. For pulse widths comparable with PAM (30 ns) and fluence operating at the ANSI safety limit, the NEN for $r = 1 \mu\text{m}$ is 292, which is a lower NEN than typically reported in PAM. This number can be further decreased by increasing the fluence or shortening the pulse.

3 Methods

3.1 Sample Selection

To demonstrate the imaging capabilities of nPAT, we chose simulation geometries based on x-ray microscopy image data obtained and generously provided by Dr. Saibil of Hale et al.³⁹ We chose these samples, because they were obtained with x-ray microscopy and can serve as extremely high-resolution digital phantoms for physical simulations. Also, these samples show the malaria parasites clearly, in addition to the parasitophorous vacuole, digestive vacuole, and RBC membrane. The samples

also show the RBC at different life cycle stages. The simulation geometries are outlined below.

3.2 Simulation Geometry

We performed simulations on experimental data obtained by Hale et al.³⁹ via soft x-ray microscopy. These images depict a malaria-infected RBC treated with the broad-spectrum cysteine protease inhibitor E64. This treatment allows for the rupture of the parasitophorous vacuole membrane (PVM) but prevents RBC membrane rupture. The end result is merozoites that would otherwise egress, being trapped in the RBC.^{40,41}

These tomograms could then be used to construct a simulation geometry that was suitable for the photoacoustic imaging of the specimen. A sample slice from the segmented tomogram is shown in Fig. 1(a). This slice was transformed into a simulation geometry by filling in the segmented regions and assigning to each color a different absorption coefficient. A sample slice of the resultant geometry is shown in Fig. 1(b), along with the axially focused laser beam and the direction in which it scans. Scanning along the slice yields a series of 1-D images that can be combined and segmented to form a 2-D image. This can be repeated over the entire 3-D x-ray tomogram to yield a series of 2-D images, which can be combined into a 3-D image. Hale et al.³⁹ also used x-ray microscopy to image earlier stage malaria within RBCs by fixing with selective PKG inhibitor compound 2 (C2) to reversibly inhibit egress prior to the rounding up stage. These 3-D tomograms could also be similarly utilized and segmented to simulate nPAT imaging of malaria at this earlier stage. We performed simulations on this geometry in the same way as outlined above for the E64 fixed schizonts. The C2 tomograms consisted of 43 slices, and the E64 tomograms consisted of 27 slices. For both geometries, the distance between each slice was 80 nm and the pixel size in each slice was 16×16 nm.

3.3 Wave Propagation

Once the simulation geometry was created, the k-wave^{42,43} toolbox in MATLAB was used to simulate the propagation of all waves throughout the simulation. This toolbox solves the photoacoustic wave equation in both time and space using

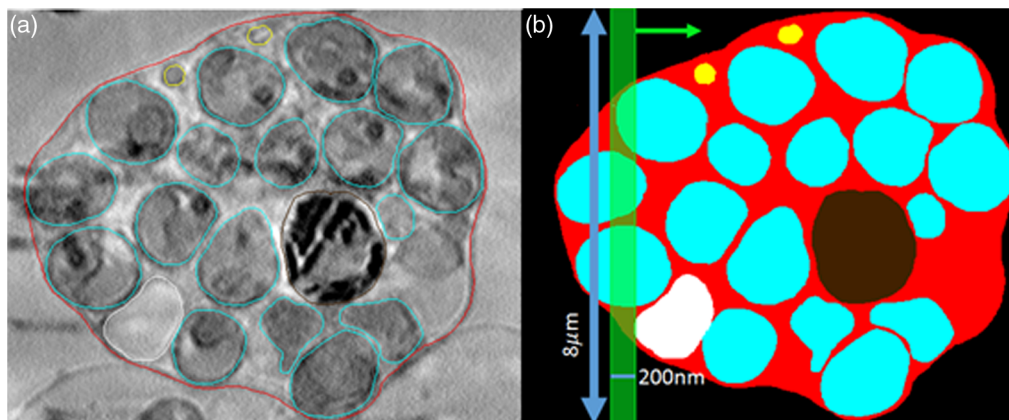


Fig. 1 (a) Segmented slice from E64 treated RBC infected with malaria imaged with x-ray microscopy, (b) simulation geometry slice showing the laser spatial dimensions and scan direction; each color of the RBC is assigned a different absorption coefficient. Green bar represents the laser, and green arrow is the scanning direction. Cyan: merozoite membrane, yellow: PVM, brown: digestive vacuole, red: RBC membrane, and white: additional vacuole, as identified by Hale et al.³⁹

a pseudospectral method and therefore allows for the modeling of acoustic wave propagation in a user-friendly and computationally efficient manner.

The k-wave simulation was run in 2-D for the E64 simulation model to conduct slice-by-slice imaging of the RBC. The detector was placed at the top of the excitation laser pulse. To simulate a focused probe beam of 200 nm, signals arriving at a detector array at the top of the laser beam in Fig. 1(b) were averaged in time to yield a single waveform. The resulting pressure versus time A-line scans were set beside one another for the reconstruction of initial pressure in each slice for simple morphological imaging. Following this, the resulting images were manually segmented to obtain outlines of the differentiable merozoites and RBC membrane. For functional imaging, the detected pressures were corrected for r^2 amplitude decay using a correction algorithm.⁴⁴ This was not done for morphological images because the contrast was suitable for segmentation without this correction, and the raw pixel values do not reveal any morphological information. The pressures were assumed to be higher in the cytoplasm than in the parasites themselves as the cytoplasm contains the most Hb. For functional imaging, Hz amplitude was assumed to be 10 times that of the cytoplasm amplitude,⁴⁵ with little to no initial pressure in the parasites (corresponding to low absorber concentration).

3.4 Functional Imaging Parameters and Geometry

To simulate functional imaging, we have replicated conditions in which the Hz and Hb concentrations are not uniform throughout the cell, with Hz only present in the digestive vacuole of the parasites. We have simulated nPAT RBC imaging at two different wavelengths, one at which Hb and Hz both absorb strongly and another at which only Hz absorbs strongly.

The reason for difference imaging is that Hb optical absorption is strong at 532 nm; however, Hz absorption can be more than an order of magnitude higher than Hb at this wavelength.^{45–47} Therefore, if Hz were evenly distributed throughout the RBC, it would be the only optical absorber that stands out as compared with the background and would render Hb concentration mapping impossible. Fortunately, Hz formation and storage occurs

entirely inside the digestive vacuole of the cell.⁴⁸ Additionally, Hb absorption is around four orders of magnitude less than that of Hz at wavelengths of around 670 nm. Therefore, PA signals imaging at 670 nm would almost entirely originate from Hz. The drastic difference in Hb absorption at these two wavelengths (532 and 670 nm), and the strong absorption of Hz at both of these wavelengths, presents an opportunity for difference imaging. Our simulations have been performed accordingly, with one simulation featuring both Hz and Hb absorptions, and a second image featuring only Hz absorption. The difference between these two images reveals the Hb concentration distribution throughout the cell.

4 Results

4.1 Morphological Imaging

X-ray tomograms of E64 treated schizonts just prior to egress were used as the simulation geometry to determine the initial acoustic pressure, which was then allowed to propagate to a linear detector array with element size of 200 nm (corresponding to the diffraction limit of 532-nm light, representing the focused probe beam). For the sake of simplicity, detected A lines were converted to images by simply mapping the intensity of the detected waveforms back onto the image space. These images were in turn manually segmented to identify parasites within the cell. The maximum supported frequency of the grid was 46.7864 GHz, and the detectors were not given any restrictions on bandwidth to simulate the high bandwidth of the pump-probe detection. This is in contrast to a PAM simulation, in which the detectors would have to be assigned some bandwidth of detection. This high bandwidth is what allows nPAT to achieve higher resolutions suitable for cellular imaging. The output of the k-wave simulation (a series of pressure versus time plots) represents detected signals in nPAT at different positions of laser scanning.

A 2-D slice from a simulated nPAT image is shown in Fig. 2(b). This figure shows that the merozoite images in nPAT have comparable resolution to those in x-ray microscopy. Merozoites (manually outlined in blue) are clearly visible within the RBC membrane (outlined in red). However, if this image

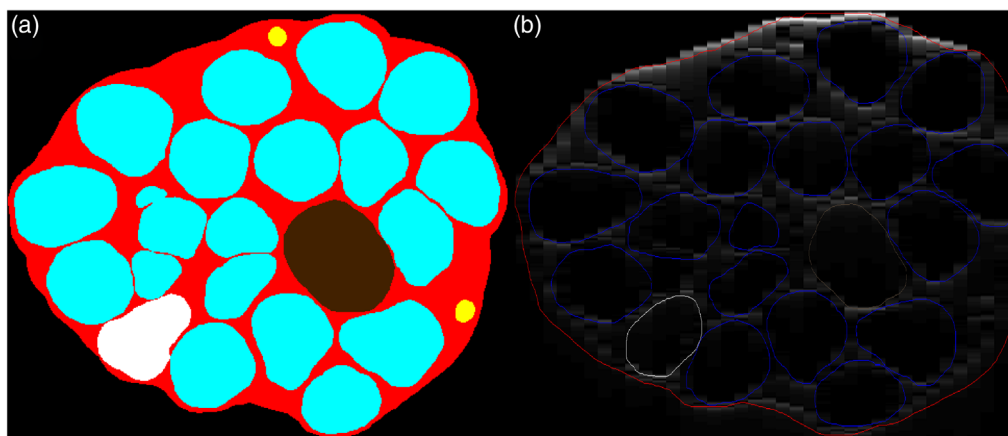


Fig. 2 Simulation 2-D output (a) simulation geometry from segmented x-ray micrographs provided by Hale et al.³⁹ and (b) nPAT simulated image of samples slice in (a); outlines of merozoites and RBC can be made, as well as the larger vacuoles. Manual segmentation was performed to the image in order to outline key features.

was obtained by an nPAT imaging device, it would be an *in-vivo* image of the merozoites without necessitating fluorescent labeling. In addition, two of the vacuoles identified by Hale et al. are also visible.³⁹

This image was generated assuming Hb concentrations in the RBC according to the biological parameters. It has been shown that malaria cells digest up to 65% of the Hb in their host cell,⁴⁹ and so the absorption coefficient inside the merozoites was modeled as being ~30% smaller than that of the surrounding cytoplasm. Although the actual Hb may well be broken down and sent to the digestive vacuole for biocrystallization into Hz, the ultimate effect of this difference is that there is a much weaker photoacoustic signal from the malarial cells as opposed to the cytoplasm because that they have far less Hb.⁵⁰ This contrast is present regardless of where the Hb ends up as long as there is less Hb inside the merozoites than inside the cytoplasm. Hb that enters the merozoites is broken down via proteolysis, and the waste products are in turn transported to the digestive vacuole.^{49,50} It is reasonable to expect that the Hb concentration inside merozoites will be substantially lower than that in the cytoplasm. nPAT can, therefore, differentiate between subcellular merozoites in malaria-infected RBCs and the cytoplasm of the RBC. As Hz is localized in the digestive vacuole (which can be removed via subtraction imaging at a different wavelength), the absorption of Hz was ignored for anatomical imaging simulations. However, it should be noted that in the experiment the suppression of this background will require multiwavelength laser imaging, taking advantage of the large difference in absorption of Hz and Hb at the wavelength of 700 nm and comparing with images from wavelengths at which Hb exhibits a peak. It can be seen that the stronger signals are near the “edge” of the merozoites. This is not to be confused with an edge effect; however, this is a consequence of the tight packaging of merozoites at this stage. The erythrocyte cytoplasm is visible entirely and all parts of it produce a signal. The appearance of signals originating from membranes alone is due to the high density of merozoites in the cell. As Hb concentration inside the merozoites is modeled to be smaller than that of the cytoplasm, the absence of a signal is used to identify merozoites. Merozoites are tightly packed within the cell, these signals are only strong in the small areas between merozoites, leading to what appears to be an edge effect but is in fact simply Hb absorption.

Two-dimensional slice-by-slice imaging can enable 3-D imaging and rendering of biological phenomenon. In this way, nPAT can achieve 3-D imaging through repeated tomographic imaging of 2-D slices. These 2-D slices can be segmented and then a mesh can be formed from segmented features to render 3-D images. The E64 nPAT tomogram was put through this process to model a sample nPAT 3-D image. The resultant image (shown in Fig. 3) was generated by meshing segmented merozoites, vacuoles, and the RBC membrane.

The shapes of the merozoites are apparent in high resolution. This image displays the 3-D imaging capabilities of nPAT to image malaria-infected RBCs. As nPAT is a noninvasive test, this imaging could theoretically be done during the live development of malaria without the need for E64 fixation to prevent egress, allowing for visualization of malarial development in living RBCs. The primary constraint of *in vivo* imaging will be in obtaining a high signal-to-noise ratio while simultaneously achieving fast raster scanning to allow for dynamic visualization. In this context, fast pump-probe scanning techniques

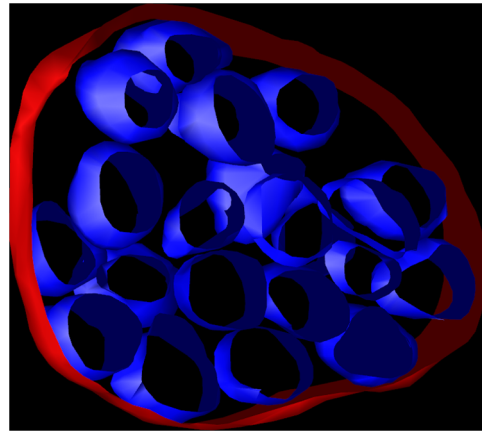


Fig. 3 E64 simulated 3-D nPAT image after slice segmentation and meshing: merozoites (blue) can be easily distinguished. The RBC outline (red) is also visible. The 3-D tomogram shows structural features with nanometer resolution throughout the RBC.

such as asynchronous optical sampling can be combined with fast raster scanning techniques such as those used in photoacoustic remote sensing microscopy (PARS) to increase speeds and potentially enable dynamic imaging for small fields of views.

Different stages of malarial development can also be imaged with nPAT, allowing it to record, *in vivo* and without fluorescent labels, malarial development after cell infection. A C2 fixed cell was imaged with an x-ray microscope by Hale et al.³⁹ These tomograms, as in the E64 case, can serve as inputs to a k-wave simulation of nPAT imaging. The 2-D sample geometry with segmentation is shown in Fig. 4(a), and the resulting simulated nPAT image of this sample is subsequently shown in Fig. 4(b). It can be seen that the rough morphology of the RBC and the PVM is both preserved and visible in nPAT.

The resulting 3-D tomographic image is shown in Fig. 5. The yellow parasitophorous vacuole is clearly visible. However, the packaged malarial parasites could not be consistently differentiated from the parasitophorous vacuole in all 2-D slices. Nevertheless, the shape of the vacuole can be assumed to roughly resemble the shape of the parasites themselves as demonstrated by Hale et al.³⁹ This image demonstrates that nPAT is capable of imaging not just late stage but also early stage malarial development *in vivo*.

4.2 Functional Imaging

Figure 6(a) shows the resulting image from functional imaging simulations at a wavelength where Hb and Hz absorb strongly. Due to the even stronger absorption of Hz, it can be seen that there is little contrast near the digestive vacuole from Hb, and the cell appears very dim compared with the strong signal coming from the digestive vacuole. Imaging at a wavelength where only Hz absorbs will essentially only produce an image of Hz concentration itself as shown in Fig. 6(b). To see the Hb image with the Hz interference removed, subtraction imaging can be done by taking the difference between Figs. 6(a) and 6(b), which is shown in Fig. 6(c). With the Hz signal subtracted, Fig. 6(c) is a relative concentration map of Hb only, therefore demonstrating the functional information that can be obtained from nPAT.

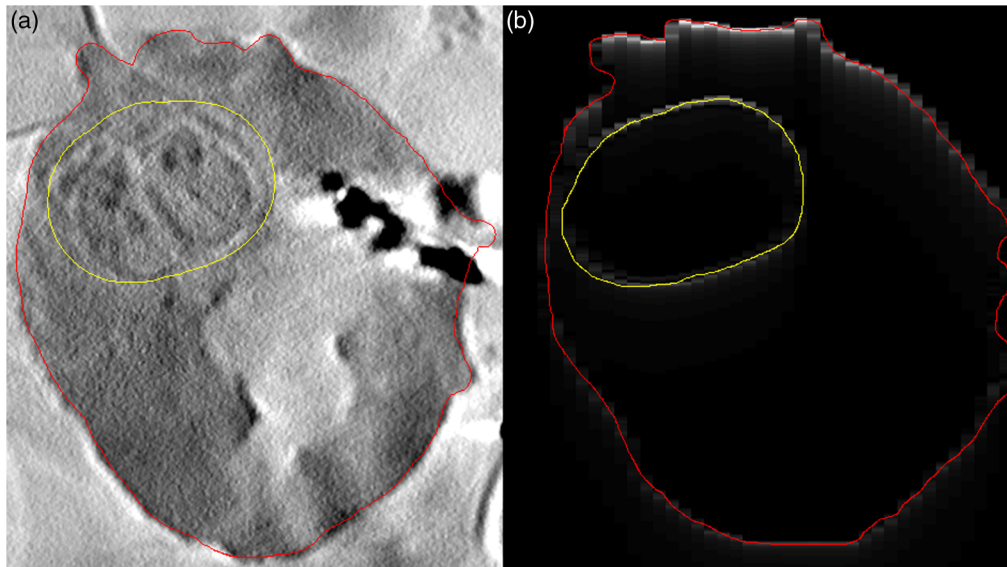


Fig. 4 (a) Segmented slice from C2 treated RBC infected with malaria imaged with x-ray microscopy, (b) simulated and segmented nPAT image of (a); outlines of the PVM and RBC membrane are visible (yellow: PVM, red: RBC membrane).



Fig. 5 Three-dimensional image of C2 fixed schizont after slice segmentation and meshing, demonstrating nPAT's high-resolution imaging of early stage malarial development. Parasitophorous vacuole is shown in yellow with RBC membrane shown in red.

5 Discussion

The theoretical sensitivity and resolution of nPAT were derived. The sensitivity value of 292 NEN and 21 Pa NEP can be expected to be that of an ideal nPAT system. This would imply that a signal of typical amplitudes should be detectable. It has been previously shown by simulation that a 100 W, 7-ps pulse is capable of generating photoacoustic pressures on the order of 10^4 Pa.³⁴ This sensitivity value demonstrated that nPAT should be capable of detecting signals generated from RBCs for high-resolution imaging. The primary factor affecting the sensitivity is the distance from the probe focus. The sensitivity will decrease as distance from the sample increases. However, the distance between the probe and pump will typically be in the range of μm , which is substantially closer to detection that is feasible with a transducer as in PAM. Therefore, nPAT is expected to still maintain low NEP at imaging depths of several microns.

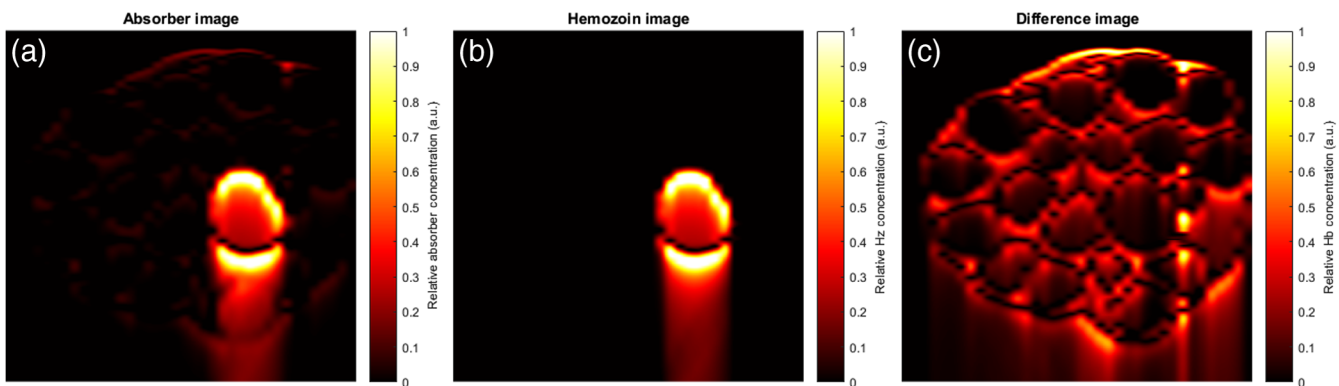


Fig. 6 Simulated functional imaging via nPAT. (a) Full absorber image, including both Hb and Hz. (b) Hz image showing relative concentration map. (c) Difference image of subtracting (b) from (a), revealing relative Hb concentration in the cell.

The propagation of nPAT signals is dependent on two factors, one of which is the $\propto r^{-3}$ amplitude decay of all 3-D acoustic waves. The amplitude of the wave must not fall below the system sensitivity at the time and location of detection. The second limitation is that of acoustic frequency attenuation. As an acoustic wave travels through a medium, higher frequencies are attenuated more as compared with lower frequencies in accordance with power-law attenuation. This places a limitation on the maximum detectable frequency of the pump-probe method since signals, as they propagate, will lose their high-frequency components that are crucial for higher resolution imaging. As a result, the actual resolution is itself a function of the imaging depth, with smaller imaging depths corresponding to higher resolutions (with an upper limit on resolution as derived earlier for entirely superficial imaging). nPAT is unique in this context from transducer-based photoacoustic imaging modalities since in nPAT, the detection beam is focused close to the point of optical generation. Therefore, imaging resolution does not depend on the acoustic time-of-flight distance from the source to the surface of the sample but rather the time-of-flight from the source to the probe beam focus. The imaging depth, therefore, depends on light penetration into the sample. So long as the probe beam light can reflect back from its focal point at a given depth, nPAT imaging is possible. The detection laser can be focused at a point 8 m away from the excitation point so that the acoustic signal needs only travel distance between the two laser foci.

The maximum achievable resolution was derived to be ~ 10 nm at a pulse duration of 7 ps. Narrower pulse widths will produce higher frequency signals, which, if detectable, can extend the maximum achievable resolution of nPAT to smaller than this value (assuming an indefinitely small absorber). About 10 nm represents the superficial resolution of nPAT, and is calculated assuming that the distance from generation to detection is very small so as to not heavily attenuate high frequencies within the signal. nPATs resolution also depends on the absorbers in question and their physical size, with a limit on resolution corresponding to the size of the absorber itself. The experimental resolution of nPAT will degrade at larger detection distances from the source due to frequency attenuation in the sample and thermal nonlinearities. Thermal nonlinearities can be negated so long as the rise in temperature is kept small, and we have demonstrated in previous studies that the temperature rise from nPAT should be in the mK range.³⁴ Our simulations have accounted for frequency attenuation of the signals ($\alpha = 0.0022$, power-law attenuation with exponent of 2) and have shown that high-resolution imaging of RBCs is still possible for depths up to at least 8 μm . Therefore, it is believed that the frequency attenuation of the acoustic signal will not result in a large enough degradation of the resolution to no longer be suitable for subcellular resolution imaging. However, precise estimates of the ranges of resolution and sensitivity will require more intensive simulation studies examining the precise full width at half maximum of a photoacoustic signal as it travels through a sample at various imaging depths and at various pulse widths. It is also important to note that nPAT serves to improve the axial resolution, but the lateral resolution of nPAT remains diffraction limited. To achieve true 3-D super-resolution imaging, a future generation of nPAT could integrate concepts from structured illumination⁵¹ to achieve lateral super-resolution, and integrate these principles with the axial super-resolution achieved by

pump-probe imaging. Therefore, nPAT can serve as a key component in the realization of a truly 3-D super-resolution microscopy.

Previous studies have already demonstrated in experiment the feasibility of photoacoustic signal detection through the use of laser beams, leading to the development of methods such as PARS microscopy.^{52,53} However, the detection bandwidth of PARS is ultimately dependent on the bandwidth of a detector photodiode, which is typically not in the range of several GHzs. This is a result of the fact that the probe beam in PARS is not pulsed but continuous. Using a pulsed probe and pump beam, as in picosecond ultrasonics,²⁵ can increase the detection bandwidth in the range of hundreds of GHz, depending on the minimum possible delay increment between the pump and probe beams.

The experimental setup of nPAT is described in our previous study.²⁴ In brief, nPAT consists of confocal pump and probe laser beams, one that generates the signal and the other that detects it. The probe beam is focused at the point where detection is desired (usually on the surface of the sample). Through the use of a mechanical optical delay line, the timing between arrival of the two pulses can be carefully controlled, allowing for signal detection in bandwidths in the range of hundreds of GHz. Currently, the time taken for a scan of a single A-line is several hours, which is not practical for use. The primary time limiting step is the slow mechanical scanning of the optical delay line. However, the delay-line can be replaced in future generations of the system with asynchronous optical sampling techniques, which can achieve single delay scans in ≤ 1 s.

nPAT can theoretically image any molecules within biological samples that strongly absorb a particular wavelength of laser light at high contrast levels to the background. This is largely due to the high versatility of optical absorption spectra in biological samples. As the acoustic signal in nPAT is ultimately proportional to the absorption coefficient, nPAT allows for the visualization of a multitude of biological molecules on par with those previously imaged by photoacoustic imaging; this includes Hb,^{54,55} lipids,⁵⁶ melanin,⁵⁷⁻⁵⁹ and water.⁶⁰

The contrast mechanism for an nPAT image is, as in photoacoustic imaging, optical absorption. In this way, nPAT can yield intrinsic optical absorption information in the case where a sample strongly absorbs the excitation laser wavelength. The excitation wavelength can in turn be adjusted to image using different intrinsic contrast agents and obtain a multitude of optical absorption maps for different wavelengths. In the context of imaging RBCs, an excitation wavelength of choice is 532 nm, as Hb has an absorption peak here. Different intrinsic contrast agents can be selected by tuning the excitation laser to the absorption peak (as compared with other locally occurring absorbers) of the molecule of interest.

Our simulations show the potential for nPAT to image cells at resolutions comparable with x-ray microscopes. However, unlike x-ray microscopy, an nPAT image would not expose the sample to damaging ionizing radiation. In addition, nPAT imaging of RBCs does not require any sample preparation. This is because the primary absorber in RBCs is Hb, which is already naturally occurring. As a result, Hb concentration mapping can be performed by nPAT without the need to prepare or otherwise alter the sample. Our simulations also indicate that nPAT has the ability to image malarial cells at different stages of parasitic development. Our simulations suggest that nPAT has the potential to achieve anatomical and functional *in vivo*

imaging at resolutions comparable with x-ray microscopy without using exogenous contrast agents.

While currently under development, the results here demonstrate the potential of nPAT to impact biomedical imaging. We believe that this imaging modality can eventually enable label-free 3-D imaging at high resolutions. Nevertheless, further research is required to experimentally develop nPAT to achieve its first nanoscale images of real samples.

Disclosures

The authors have no relevant financial interests in this article and no potential conflicts of interest to disclose.

Acknowledgments

Some of the computing for this project was performed at the OU Supercomputing Center for Education & Research (OSKER) at the University of Oklahoma. OSKER System Administrator Kali McLennan provided valuable technical expertise. The authors gratefully acknowledge the PHF Team Science Grant Program and Diabetes CoBRE Pilot Project from the University of Oklahoma Health Sciences Center, and the College of Engineering at the University of Oklahoma, for funding.

References

- R. Kasper et al., "Single-molecule STED microscopy with photostable organic fluorophores," *Small* **6**, 1379–1384 (2010).
- F. Cella Zanacchi et al., "Live-cell 3D super-resolution imaging in thick biological samples," *Nat. Methods* **8**, 1047–1049 (2011).
- A. Danielli et al., "Label-free photoacoustic nanoscopy," *J. Biomed. Opt.* **19**(8), 086006 (2014).
- C. W. Freudiger et al., "Label-free biomedical imaging with high sensitivity by stimulated raman scattering microscopy," *Science* **322**, 1857–1861 (2008).
- M. J. Rust, M. Bates, and X. Zhuang, "Sub-diffraction-limit imaging by stochastic optical reconstruction microscopy (STORM). Stochastic optical reconstruction microscopy (STORM) provides sub-diffraction-limit image resolution," *Nat. Methods* **3**, 793–796 (2006).
- B. Huang et al., "Three-dimensional super-resolution imaging by stochastic optical reconstruction microscopy," *Science* **319**, 810–813 (2008).
- S. W. Hell et al., "The 2015 super-resolution microscopy roadmap," *J. Phys. D: Appl. Phys.* **48**(44), 443001 (2015).
- E. D'Este et al., "STED nanoscopy reveals the ubiquity of subcortical cytoskeleton periodicity in living neurons," *Cell Rep.* **10**, 1246–1251 (2015).
- E. D'Este et al., "Ultrastructural anatomy of nodes of Ranvier in the peripheral nervous system as revealed by STED microscopy," *Proc. Natl. Acad. Sci. U. S. A.* **114**, E191–E199 (2017).
- B. Dudok et al., "Cell-specific STORM super-resolution imaging reveals nanoscale organization of cannabinoid signaling," *Nat. Neurosci.* **18**, 75–86 (2015).
- O. Huber et al., "Localization microscopy (SPDM) reveals clustered formations of P-Glycoprotein in a human blood-brain barrier model," *PLoS One* **7**(9), e44776 (2012).
- L. V. Wang and S. Hu, "Photoacoustic tomography: in vivo imaging from organelles to organs," *Science* **335**, 1458–1462 (2012).
- A. M. Hammond and R. Galizi, "Gene drives to fight malaria: current state and future directions," *Pathog. Global Health* **111**, 412–423 (2018).
- A. Esposito et al., "FRET imaging of hemoglobin concentration in plasmodium falciparum-infected red cells," *PLoS One* **3**(11), e3780 (2008).
- C. D. Fitch and P. Kanjanangulpan, "The state of ferriprotoporphyrin IX in malaria pigment," *J. Biol. Chem.* **262**, 15552–15555 (1987).
- S. Pagola et al., "The structure of malaria pigment β -haematin," *Nature* **404**, 307–310 (2000).
- D. J. Sullivan et al., "On the molecular mechanism of chloroquine's antimalarial action," *Proc. Natl. Acad. Sci. U. S. A.* **93**, 11865–11870 (1996).
- K. Y. Fong and D. W. Wright, "Hemozoin and antimalarial drug discovery," *Future Med. Chem.* **5**, 1437–1450 (2013).
- R. L. Guerrant, D. H. Walker, and P. F. Weller, *Tropical Infectious Diseases: Principles, Pathogens and Practice E-Book*, Elsevier Health Sciences, London (2011).
- S. Papadopoulos, K. D. Jürgens, and G. Gros, "Protein diffusion in living skeletal muscle fibers: dependence on protein size, fiber type, and contraction," *Biophys. J.* **79**, 2084–2094 (2000).
- E. M. Strohm, M. J. Moore, and M. C. Kolios, "Single cell photoacoustic microscopy: a review," *IEEE J. Sel. Top. Quantum Electron.* **22**, 137–151 (2016).
- E. M. Strohm and M. C. Kolios, "Classification of blood cells and tumor cells using label-free ultrasound and photoacoustics," *Cytometry Part A* **87**, 741–749 (2015).
- B. Dong, C. Sun, and H. F. Zhang, "Optical detection of ultrasound in photoacoustic imaging," *IEEE Trans. Biomed. Eng.* **64**, 4–15 (2017).
- P. Samant et al., "Nanoscale photoacoustic tomography (nPAT) for label-free super-resolution 3D imaging of red blood cells," *Proc. SPIE* **10350**, 103500P (2017).
- O. Matsuda et al., "Fundamentals of picosecond laser ultrasonics," *Ultrasonics* **56**, 3–20 (2015).
- E. Pontecorvo et al., "Visualizing coherent phonon propagation in the 100 GHz range: a broadband picosecond acoustics approach," *Appl. Phys. Lett.* **98**, 011901 (2011).
- T. Pezeril et al., "Optical generation of gigahertz-frequency shear acoustic waves in liquid glycerol," *Phys. Rev. Lett.* **102**, 107402 (2009).
- R. J. Smith et al., "Parallel detection of low modulation depth signals: application to picosecond ultrasonics," *Meas. Sci. Technol.* **19**(5), 055301 (2008).
- A. Bartels et al., "Ultrafast time-domain spectroscopy based on high-speed asynchronous optical sampling," *Rev. Sci. Instrum.* **78**, 035107 (2007).
- C. Zhang et al., "In vivo photoacoustic microscopy with 7.6-mm axial resolution using a commercial 125-MHz ultrasonic transducer," *J. Biomed. Opt.* **17**, 116016 (2012).
- S.-L. Chen, L. J. Guo, and X. Wang, "All-optical photoacoustic microscopy," *Photoacoustics* **3**, 143–150 (2015).
- J. Yao and L. V. Wang, "Sensitivity of photoacoustic microscopy," *Photoacoustics* **2**, 87–101 (2014).
- C. Zhang et al., "Ultrabroad bandwidth and highly sensitive optical ultrasonic detector for photoacoustic imaging," *ACS Photonics* **1**, 1093–1098 (2014).
- P. Samant, J. Chen, and L. Xiang, "Characterization of the temperature rise in a single cell during photoacoustic tomography at the nanoscale," *J. Biomed. Opt.* **21**(7), 075009 (2016).
- I. G. Calasso, W. Craig, and G. J. Diebold, "Photoacoustic point source," *Phys. Rev. Lett.* **86**, 3550–3553 (2001).
- S. H. Jack, D. B. Hann, and C. A. Greated, "Influence of the acousto-optic effect on laser Doppler anemometry signals," *Rev. Sci. Instrum.* **69**, 4074–4081 (1998).
- A. Giulietti and K. Ledingham, *Progress in Ultrafast Intense Laser Science*, Springer Science & Business Media, Berlin, Heidelberg (2010).
- W. Xia et al., "An optimized ultrasound detector for photoacoustic breast tomography," *Med. Phys.* **40**, 032901 (2013).
- V. L. Hale et al., "Parasitophorous vacuole poration precedes its rupture and rapid host erythrocyte cytoskeleton collapse in Plasmodium falciparum Egress," *Proc. Natl. Acad. Sci. U. S. A.* **114**, 3439–3444 (2017).
- S. Glushakova et al., "Irreversible effect of cysteine protease inhibitors on the release of malaria parasites from infected erythrocytes," *Cell. Microbiol.* **11**, 95–105 (2009).
- R. Chandramohanadas et al., "Apicomplexan parasites Co-Opt host calpains to facilitate their escape from infected cells," *Science* **324**, 794–797 (2009).
- B. E. Treeby and B. T. Cox, "K-Wave: MATLAB toolbox for the simulation and reconstruction of photoacoustic wave fields," *J. Biomed. Opt.* **15**(2), 021314 (2010).

43. B. E. Treeby et al., "Modeling nonlinear ultrasound propagation in heterogeneous media with power law absorption using a k-space pseudospectral method," *J. Acoust. Soc. Am.* **131**, 4324–4336 (2012).
44. I. Pelivanov et al., "High resolution imaging of impacted CFRP composites with a fiber-optic laser-ultrasound scanner," *Photoacoustics* **4**, 55–64 (2016).
45. Y. A. Menyayev et al., "Preclinical photoacoustic models: application for ultrasensitive single cell malaria diagnosis in large vein and artery," *Biomed. Opt. Express* **7**, 3643–3658 (2016).
46. J. L. Burnett, J. L. Carns, and R. Richards-Kortum, "In vivo microscopy of hemozoin: towards a needle free diagnostic for malaria," *Biomed. Opt. Express* **6**, 3462–3474 (2015).
47. C. Cai et al., "In vivo photoacoustic flow cytometry for early malaria diagnosis," *Cytometry Part A* **89**, 531–542 (2016).
48. S. Kapishnikov et al., "Oriented nucleation of hemozoin at the digestive vacuole membrane in *Plasmodium falciparum*," *Proc. Natl. Acad. Sci. U. S. A.* **109**, 11188–11193 (2012).
49. L. M. Coronado, C. T. Nadovich, and C. Spadafora, "Malarial hemozoin: from target to tool," *Biochim. Biophys. Acta* **1840**, 2032–2041 (2014).
50. D. E. Goldberg et al., "Hemoglobin degradation in the malaria parasite *Plasmodium falciparum*: an ordered process in a unique organelle," *Proc. Natl. Acad. Sci. U. S. A.* **87**, 2931–2935 (1990).
51. T. W. Murray et al., "Super-resolution photoacoustic microscopy using blind structured illumination," *Optica* **4**, 17–22 (2017).
52. P. Hajireza et al., "Non-interferometric photoacoustic remote sensing microscopy," *Light Sci. Appl.* **6**, e16278 (2017).
53. K. L. Bell et al., "Temporal evolution of low-coherence reflectometry signals in photoacoustic remote sensing microscopy," *Appl. Opt.* **56**, 5172–5181 (2017).
54. S. E. Bohndiek et al., "Photoacoustic tomography detects early vessel regression and normalization during ovarian tumor response to the anti-angiogenic therapy Trebananib," *J. Nucl. Med.* **56**, 1942–1947 (2015).
55. J. Laufer et al., "In vivo preclinical photoacoustic imaging of tumor vasculature development and therapy," *J. Biomed. Opt.* **17**(5), 056016 (2012).
56. J. A. Guggenheim et al., "Photoacoustic imaging of human lymph nodes with endogenous lipid and hemoglobin contrast," *J. Biomed. Opt.* **20**(5), 050504 (2015).
57. H. F. Zhang et al., "Functional photoacoustic microscopy for high-resolution and noninvasive in vivo imaging," *Nat. Biotechnol.* **24**, 848–851 (2006).
58. J.-T. Oh et al., "Three-dimensional imaging of skin melanoma in vivo by dual-wavelength photoacoustic microscopy," *J. Biomed. Opt.* **11**(3), 034032 (2006).
59. I. Stoffels et al., "Metastatic status of sentinel lymph nodes in melanoma determined noninvasively with multispectral photoacoustic imaging," *Sci. Transl. Med.* **7**, 317ra199 (2015).
60. Z. Xu, Q. Zhu, and L. V. Wang, "In vivo photoacoustic tomography of mouse cerebral edema induced by cold injury," *J. Biomed. Opt.* **16**(6), 066020 (2011).

Pratik Samant is a PhD candidate of biomedical engineering at the University of Oklahoma. Currently, he is developing novel photoacoustic and x-ray acoustic imaging methods for use in biomedical contexts.

Liangzhong Xiang is an assistant professor in the School of Electrical and Computer Engineering at the University of Oklahoma. He has published more than 50 peer-reviewed journal articles and delivered 20 invited talks. He has served as a grant reviewer for the Department of Energy and other agencies. His laboratory invented/discovered x-ray induced acoustic tomography (XACT) and electroacoustic tomography (EAT).

Biographies for the other authors are not available.